Automatic segmentation of human brain sulci

Faguo Yang, Frithjof Kruggel *

Signal and Image Processing Laboratory, Department of Biomedical Engineering, University of California, Irvine, CA 92697-2755, United States

Abstract

The neocortical surface has a rich and complex structure comprised of folds (gyri) and fissures (sulci). Sulci are important macroscopic landmarks for orientation on the cortex. A precise segmentation and labeling of sulci is helpful in human brain mapping studies relating brain anatomy and function. Due to their structural complexity and inter-subject variability, this is considered as a non-trivial task. An automatic algorithm is proposed to accurately segment neocortical sulci: vertices of a white/gray matter interface mesh are classified under a Bayesian framework as belonging to gyral and sulcal compartments using information about their geodesic depth and local curvature. Then, vertices are collected into sulcal regions by a watershed-like growing method. Experimental results demonstrate that the method is accurate and robust.

1. Introduction

The macrostructure of the human neocortex is a highly complex and convoluted surface comprised of folds (gyri) and fissures (sulci) (see Fig. 1). The development of high resolution and high contrast MR imaging techniques allows studying morphological variability of the neocortical folding patterns. The accurate segmentation of cortical sulci has many applications such as localizing activation sites precisely in functional imaging (Mangin et al., 1995), providing landmarks for 3D deformable brain image volume registration, and studying region-dependent patterns of diseases affecting the neocortex.

Two main strategies were pursued for the analysis of the cortical surface. The first employs feature-based elastic registration and warps a pre-labeled template to a subject's imaging data for segmenting and identifying anatomical structures (Behnke et al., 2003; Desikan et al., 2006). The second strategy tries to directly extract or recognize sulci in the space of an individual subject without elastic registration (Mangin et al., 1995; Goualher et al., 1997, 1999; Vaillant and Davatzikos, 1997; Lohmann and von Cramon, 2000; Rettmann et al., 2002). While the first approach has demonstrated a successful identification of some major sulci, due to the high inter-subject variability, a registration method cannot exactly match all surface features between a subject and a pre-labeled template – and it is an open question whether such a match exists (Cachia et al., 2003).

Working in the individual data space, it is possible to extract sulci directly in the image space from the 3D MR image volumes (Mangin et al., 1995; Goualher et al., 1997; Lohmann, 1998; Lohmann and von Cramon, 2000; Zhou et al., 1999; Riviére et al., 2002), or to detect them on cortical surface meshes reconstructed from 3D MR images (Khaneja et al., 1998; Rettmann et al., 2002; Vivodtzev et al., 2003; Kao et al., 2007). Although mesh-based methods require extra steps for their creation, specific surface properties may be imposed (e.g., topological constraints, no self-intersections, or surface–surface contacts) that are advantageous for segmentation. Surface features such as curvature (Vivodtzev et al., 2003) are more reliably computed, and multi-resolution schemes are much easier to implement in order

---

* Corresponding author. Tel.: +1 949 824 3729; fax: +1 949 824 1727.
  E-mail addresses: faguoy@uci.edu (F. Yang), fkruggel@uci.edu (F. Kruggel).
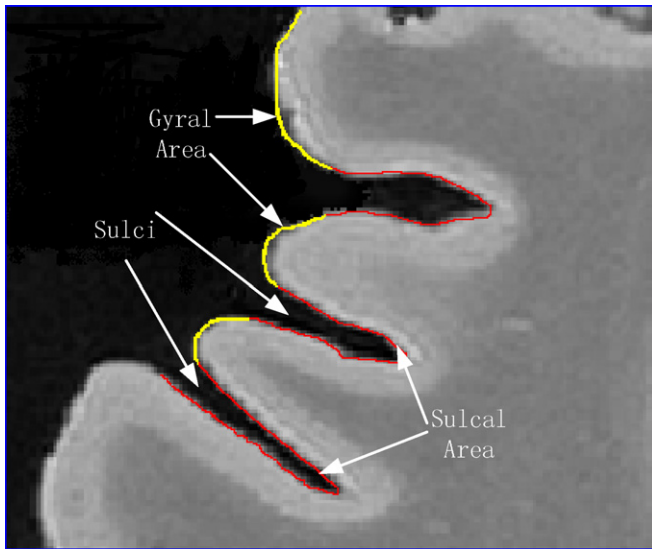
Fig. 1. A cross-section of the cortical surface.

to increase the robustness and computational efficiency. Sulci may be represented as regions (Rettmann et al., 2002) or fundus lines (Kao et al., 2007; Shi et al., 2007). It was argued that sulcal fundi are more stable in terms of definition and identification compared to sulcal regions. Our primary aim is to introduce a parcellation on the neocortex to allow morphometry, so we focus on segmenting regions.

The two main features employed for parcellating the neocortical surface are curvature (Goualher et al., 1999; Cachia et al., 2003; Vivodtzev et al., 2003) and geodesic depth (Rettmann et al., 2002; Kao et al., 2007). Curvature-based approaches make the first-order approximation that sulci are concave and gyri are convex. However, secondary structures, correlates of acquisition noise, and modeling errors may violate this assumption locally. Therefore, curvature-based algorithms may produce unwanted results, e.g., at small bridging gyri deep in cortical folds. Smoothing the surface is a viable option, but specifying the amount of smoothing is not a well-defined problem. Approaches based on geodesic depth use ad hoc techniques to distinguish sulci and gyri. Kao et al. (2007) apply depth thresholding to extract sulcal regions. Rettmann et al. (2002) use a deformable model to distinguish sulci and gyri. However, parameters describing the elasticity of the deformable model affect the definition of sulcal areas.

We suggest to combine both geodesic depth and curvature information in a Bayesian framework to classify surface vertices into sulcal and gyral compartments. Hereby, we can resolve issues of noisy surfaces, bridging gyri deep in cortical folds, and arbitrary depth thresholds. In a second step, we form sulcal regions by employing a watershed-like region growing method on the surface mesh.

2. Algorithms

Now, we discuss the key steps of our algorithm in detail: (1) surface generation and feature computation, (2) vertex classification, and (3) watershed-like growing and segment merging as sulcal regions.

2.1. Surface and feature extraction

To study the human cortex folding patterns, we may either use the interface between gray matter (GM) and cerebro-spinal fluid (CSF) or the interface between white matter (WM) and gray matter (GM) as long as the cortical surface representation is reliable (Cachia et al., 2003). However, the partial volume effects makes sulcal banks indistinguishable for tightly packed sulcal regions on the GM/CSF interface at the standard MR imaging resolution (Han et al., 2004). Therefore, it is more difficult to obtain a correct GM/CSF surface (Mangin et al., 1995). Without loss of generality, we select the WM/GM interface here for generating the cortical surface easily and reliably.

2.1.1. Surface generation
Extracting the brain's surface as a polygonal mesh from magnetic resonance imaging data of the human head is considered a complex, but well developed methodology in medical image processing. In principle, any published method may be used to obtain a triangulated mesh representing the WM/GM interface that is required for our segmentation method. However, it must be ensured that (1) the surface mesh has a topological genus of zero (an useful simplification of the neuroanatomy, but warranted at this spatial resolution level) and (2) is free of self-intersections. It is self-evident that self-intersecting surfaces are anatomically invalid.

We briefly outline our procedure in the following. T_1-weighted volumetric MR images were aligned with the stereotaxic coordinate system (Kruggel and von Cramon, 1999) and interpolated to an isotropical voxel size of 1 mm using a fourth-order B-spline method. Data were corrected for intensity inhomogeneities by a fuzzy segmentation approach using three classes (Pham and Prince, 1999), yielding an intensity-corrected T_1-weighted image, and a set of three probability images. Here, each voxel contains a probability for belonging to the intensity class 0 (background and CSF), 1 (GM, facial muscles, connective tissue), and 2 (WM, fat). Data of probability class 2 are binarized by a threshold t, and treated with a morphological erosion filter using a spherical kernel of radius d to remove small bridges between the temporal lobe and the cerebellum. To remove the cerebellum, brainstem is cut by an axial plane 15 mm below the posterior commissure, and the biggest c18-connected component (Toriwaki and Yonekura, 2002) is retained as the raw WM segmentation of the cerebrum. Note that this step also removes the outer hulls of the human brain. For our data, typical parameter settings are $t = 0.65$ and $d = 1.4$. We automatically modify t and d to determine the best combination for which the remaining cerebral volume is maximal.

The resulting raw WM segmentation was refined to have a topological genus of 0 (i.e., no holes or handles).

First, the inner ventricles and other holes encompassed by WM are filled by labeling all c18′-connected components in the background and joining all but the biggest one with the initial WM segmentation. We use a variant of the procedure proposed by Shattuck and Leahy (2001) to modify the foreground object until it has a topological genus of zero.

A triangulated surface mesh was generated from the refined white matter segmentation using a version of the "Marching Cubes" algorithm that preserves the original topology (Cignoni et al., 2000). Note that the isosurface threshold for this step must range in $t \in [0.25, 0.5]$ to maintain a c18-connectivity in the foreground and yield a mesh with a topological genus of zero.

An improved representation of the WM/GM interface is obtained by treating the initial mesh as a deformable model (Kruggel, 2005). On any vertex v_0 in the mesh, internal and external forces act until a balance is achieved. The first term corresponds to an internal force that tries to center a vertex among its edge-connected neighbors v_i, $i = \{1, \ldots, n\}$:

$$v_0^{(t+1)} = w_1 \frac{1}{n_i} \sum_{i=1}^{n_i} v_i^{(t)} + w_2 \delta f\left(v_0^{(t)}\right). \tag{1}$$

The second term corresponds to an image-driven force exerted by a gradient field f. This gradient field is computed by convolving the intensity-corrected image I with a kernel based on the first derivative of a Gaussian function ∇G with standard deviation σ (Xu and Prince, 1998). This force is weighted to capture the surface within a narrow intensity range around $I_{\lim}$: $\delta = \tanh(\kappa(I(v_0) - I_{\lim}))$. Convergence is assumed if the average intensity difference $|\overline{I(v_0)} - I_{\lim}|$ drops below a pre-defined bound. For our data, we used the settings: $\sigma = 1.0$, $\kappa = 0.2$, $w_1 = 0.01$, $w_2 = 0.004$, $I_{\lim} = (\overline{I_{WM}} + \overline{I_{GM}})/2$ for the WM/GM interface. The notation $\overline{I_{XX}}$ refers to the average compartment intensity.

One of the key issues in this step is to avoid self-intersections of the surface (Gumhold et al., 2004), as this would yield an anatomically implausible result. Finally, we reduced the number of triangles to 100,000 by edge contraction (Heckbert and Garland, 1999) and split the surface mesh at the mid-sagittal plane to yield two meshes representing the WM/GM interface of each hemisphere. Note that this mesh is non-uniform, but optimally represents the original surface properties such as curvature.

2.1.2. Surface curvature

An approximation method (Sander and Zucker, 1987; Stokely and Wu, 1992) is used to compute the mean curvature h_v of each vertex on the cortical surface mesh. At each vertex v_0, we construct a local coordinate system from its unit normal vector and two orthogonal vectors $\vec{x}, \vec{y}$ on its tangent plane. Cartesian coordinates of all edge-connected neighbors v_i, $i = \{1, \ldots, n\}$ are transformed to local coordinates $\{(x_1, y_1, h_1), \ldots, (x_n, y_n, h_n)\}$. The cortical surface near vertex v_0 is approximated by a paraboloid $S(x, y) = (x, y, ax^2 + 2bxy + cy^2)$, and coefficients a, b, c are determined by least squares estimation. The computation of the mean curvature involves in the first and second principal forms of the surface (Mortenson, 1985). For the approximating paraboloid at point vertex v_0, the mean curvature can be estimated as $h_v = a + c$. Note that there are more vertices in highly curved portions, so this estimation method is self-adaptive with respect to the surface area.

2.1.3. Geodesic depth

Processing steps for computing the geodesic depth of the WM surface voxels are illustrated in Fig. 2. We start from the refined WM segmentation computed above (Fig. 2b). Because brains were aligned with the stereotaxic coordinate system, we can simply use the y–z center plane to split the left and right hemisphere (Fig. 2c). A morphological closing filter with a spherical structuring element (Maragos and Schafer, 1990) was applied to obtain an idealized smoothed surface (Fig. 2d). The exact size of the diameter is not critical as long as it is large enough to fill the sulci, we used $d = 14$ mm here. The geodesic depth of each voxel in the filled sulcal compartment was calculated with respect to this idealized smoothed surface using a constrained 3D distance transform (Borgefors, 1984). Finally, depth information is interpolated at vertex positions of the WM mesh.

2.2. Vertex classification

Consider the cortical surface mesh M consisting of vertices v_i, $i = 1, \ldots, N$. We introduce a classification C by addressing a label L_i, $i = \{1, 2\}$ to each vertex whether it belongs to a gyral or sulcal compartment based on its mean curvature h_v and geodesic depth d_v. Classification is performed by maximizing $P(C|M)$:
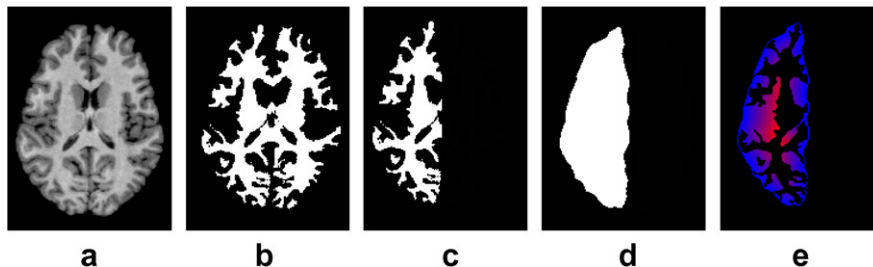

Fig. 2. Image processing steps for obtaining the sulcal geodesic depth: (a) MR image; (b) white matter; (c) splitting; (d) closing; and (e) geodesic depth.

$$C^* = \arg\max_C P(C|M) \qquad (2)$$

We assume the classification of each vertex on the cortical surface mesh is independent from each other. Therefore

$$\arg\max_C P(C|M) = \bigcup_v \arg\max_L P(L|h_v, d_v) \qquad (3)$$

This assumption highly simplifies the classification of the vertices on the cortical surface mesh. According to Bayes' rule:

$$P(L|h_v, d_v) = \frac{P(h_v, d_v|L)P(L)}{P(h_v, d_v)} \qquad (4)$$

Since $P(h_v, d_v) = \sum_L P(L)P(h_v, d_v|L)$, $P(h_v, d_v)$ is a constant for each vertex across the classes. So,

$$P(L|h_v, d_v) \propto P(L)P(h_v, d_v|L) \qquad (5)$$

We further assume that given the class label, the geodesic depth d_v and the mean curvature h_v are conditionally independent. According to this assumption, Eq. (5) becomes

$$P(L|h_v, d_v) \propto P(L)P(h_v|L)P(d_v|L) \qquad (6)$$

The density functions of each class are approximated using kernel expansion (Duda et al., 2000).

$$P(h_v|L) = \frac{1}{N_L} \sum_{i=1}^{N_L} K_{\sigma_h}(h_v - h_i) \qquad (7)$$

$$P(d_v|L) = \frac{1}{N_L} \sum_{i=1}^{N_L} K_{\sigma_d}(d_v - d_i) \qquad (8)$$

where K_{σ_h} and K_{σ_d} are Gaussian kernels with standard deviation σ_h and σ_d; h_i, d_i, $\{i = 1, \ldots, N_L\}$ correspond to samples of class L. The prior probability of each class $P(L)$ can be estimated by

$$P(L) = \frac{N_L}{N}. \qquad (9)$$

Once we know the distributions of h_v, d_v, and the prior probability $P(L)$ of each class, we can classify each vertex on the cortical surface mesh. On the other hand, if we know the class label of each vertex on the cortical surface mesh, we can use Eqs. (7)–(9) to estimate the density function $p(h_v|L)$, $p(d_v|L)$ and the prior probabilities $P(L)$. An expectation maximization (EM) algorithm is used to classify vertices:

(i) We initialize the segmentation using mean curvature only: vertices with a positive value are classified as belonging to sulci, all other as gyri. Note that the sign of the mean curvature depends on the computation method which is positive in concave regions for the method applied here.

(ii) We re-estimate density functions (Eqs. (7) and (8)) and prior probability (Eq. (9)) of each class. Parameters σ_h and σ_d are important when approximating the density functions. Larger values make the estimated density function smooth. To achieve a robust classification, we

use a strategy similar to the temperature control method in simulated annealing (Kirkpatrick et al., 1983; Aarts and Korst, 1989) to determine the values of these two important parameters:

$$\sigma_h^{(t)} = \sigma_h^{(0)} \exp(-t\alpha) \qquad (10)$$

$$\sigma_d^{(t)} = \sigma_d^{(0)} \exp(-t\alpha) \qquad (11)$$

where t is the current iteration number. In all our experiments, we used $\alpha = 1.0$, $\sigma_h^{(0)} = 0.2$, and $\sigma_d^{(0)} = 2$.

(iii) Then, we re-classify each vertex by computing $P(L)P(h_v|L)P(d_v|L)$ and addressing it to class L^* with the maximum value $P(L^*)P(h_v|L^*)P(d_v|L^*)$ among all the classes.

(iv) If the number of reclassified vertices becomes zero, or a maximum iteration number T is reached, we assume convergence and stop the classification process. Else we go to step (ii). We used $T = 20$.

Note that this method is unsupervised and training is not required.

2.3. Segmenting sulcal regions

The objective of the segmentation process is to collect vertices from the sulcal class as separate sulcal regions that correspond to neuro-biologically meaningful structures.

2.3.1. Segment growing

The watershed algorithm is widely used in the image processing literature to segment an image into catchment basins (Meyer and Beucher, 1990). Imagine puncturing holes in the local minimum of a height function and immerse the function into a pool, the water will flood areas near the local minimum, and finally form different catchment basins. The choice of the height function $f(\cdot)$ is crucial for each application. For our problem, height can be defined as (1) mean curvature, (2) geodesic depth or (3) the probability of belonging to the sulcal class (Eq. (4)). The formation of the catchment basins on the cortical surface is only affected by the topology of the vertices and their associated height values, not by their 3D vertex position. The region growing process is formalized as

(i) Create a list K of all vertices v_i of the sulcal class in descending order of their height f_i.

(ii) Starting with the highest vertex, test the labeling situation of the neighbors of v_i:
  – If all of its neighbors are unlabeled, or some of its neighbors are unlabeled and the rest of the neighbors belong to the gyral class, we create a new catchment basin.
  – If its labeled neighbors only belong to a single catchment basin, then address its label to the current vertex.
  – If its labeled neighbors belong to several different catchment basins, we search for the closest

neighboring labeled vertex v_j and address its label to the current vertex. The distance between the vertices are defined as the Euclidian distance.

Since the watershed method is sensitive to small high-frequency surface variations (e.g., detailed cortical structures), it tends to over-segment the surface. Therefore, we perform a merging process that is described in the following section.

2.3.2. Segment merging

A merging process needs a criterion for selecting candidates for merging. We use the ridge height of a basin here (see Fig. 3). Consider two neighboring segments S_i and S_j. The ridge height $r_i(S_j)$ of segment S_i with respect to segment S_j is defined as the highest geodesic depth in catchment basin S_i before spilling over into catchment basin S_j. Note that $r_i(S_j) \neq r_j(S_i)$.

The merging process is described as follows:

(i) Create a graph G in which basin segments correspond to nodes. If two segments share a common ridge, then link these neighbors by an edge.
(ii) Denote the segment depth as the maximum geodesic depth among all vertices of a segment. Create a list K of all basin segments sorted by descending depth.

 while end of list K has not been reached
  Select the current basin segment S_i as the next segment in list K.
  Collect the set $N(S_i)$ of neighbors of S_i.
  LOOP: Find the segment S_j in $N(S_i)$ that has the smallest ridge height $r_i(S_j)$.
  if $r_i(S_j)$ is smaller than a given threshold T_w
  then
   merge segments S_i and S_j.
   merge $N(S_j)$ into $N(S_i)$.
   remove S_j from $N(S_i)$ and from all neighbors of S_i.
   update the watershed information r in S_i and $N(S_i)$.
   delete segment S_j from the list K and graph G.
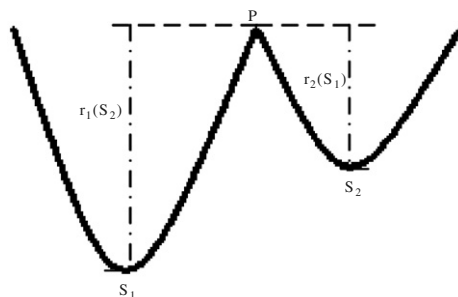 **endif**
  goto LOOP.
 endwhile

Fig. 3. An illustration of the definition of ridge height between neighboring segments.

Finally, we remove small segments without neighbors or merge them unconditionally with their largest neighbor.

3. Experiments

For an evaluation of our segmentation algorithm, we conducted a set of experiments. From a large subject database (see Kruggel, 2007 for a complete demographic description), we randomly selected 20 cases (29.4 ± 13.0 years; 8 males, 12 females). Subjects were scanned on a Bruker 3T Medspec 100 system, equipped with bird cage quadrature coil. T_1-weighted images were acquired using a 3D modified driven equilibrium Fourier transform (MDEFT) protocol: field-of-view 220 mm × 220 mm × 192 mm, matrix 256 × 256, TR = 1.3 s, TE = 10 ms, 128 sagittal slices, voxel size 0.9 mm × 0.9 mm, 1.5 mm slice thickness.

A neuroanatomist counted the number of anatomically defined segments (see Fig. 4) that make up the central (CS), post-central (PCS) and superior temporal sulcus (STS). If the number of anatomically defined segments matches the number of automatically defined segments, we consider this segmentation as correct. If our algorithm found more segments, we denote this as an over-segmentation, if less, as an under-segmentation.

In our first experiment, we assessed possible choices for the height parameter in the region growing process: (1) geodesic depth, (2) mean curvature, and (3) the sulcal class probability. We used settings of $\sigma_h^{(0)} = 0.2$, $\sigma_d^{(0)} = 2.0$ and $T_w = 2.5$ mm to obtain the segmentation results in our test sample. A neuro-anatomist counted the occurrence of under-segmentation by inspecting the lateral view of the segmented hemisphere (see Fig. 5). For height measures (2) or (3), an under-segmentation was found in 7/20 cases. No under-segmentation was found for geodesic depth that was selected as the region growing metric.
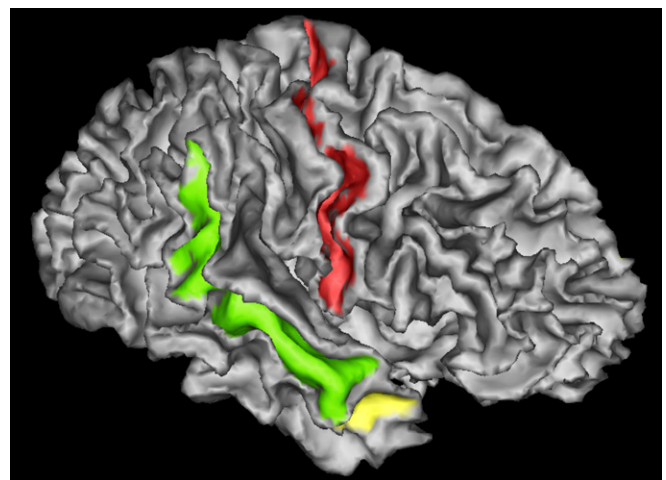

Fig. 4. An illustration of the anatomically defined segments. The central sulcus (red) only has one anatomical segment, while the superior temporal sulcus consists of two anatomical segments (yellow and green).
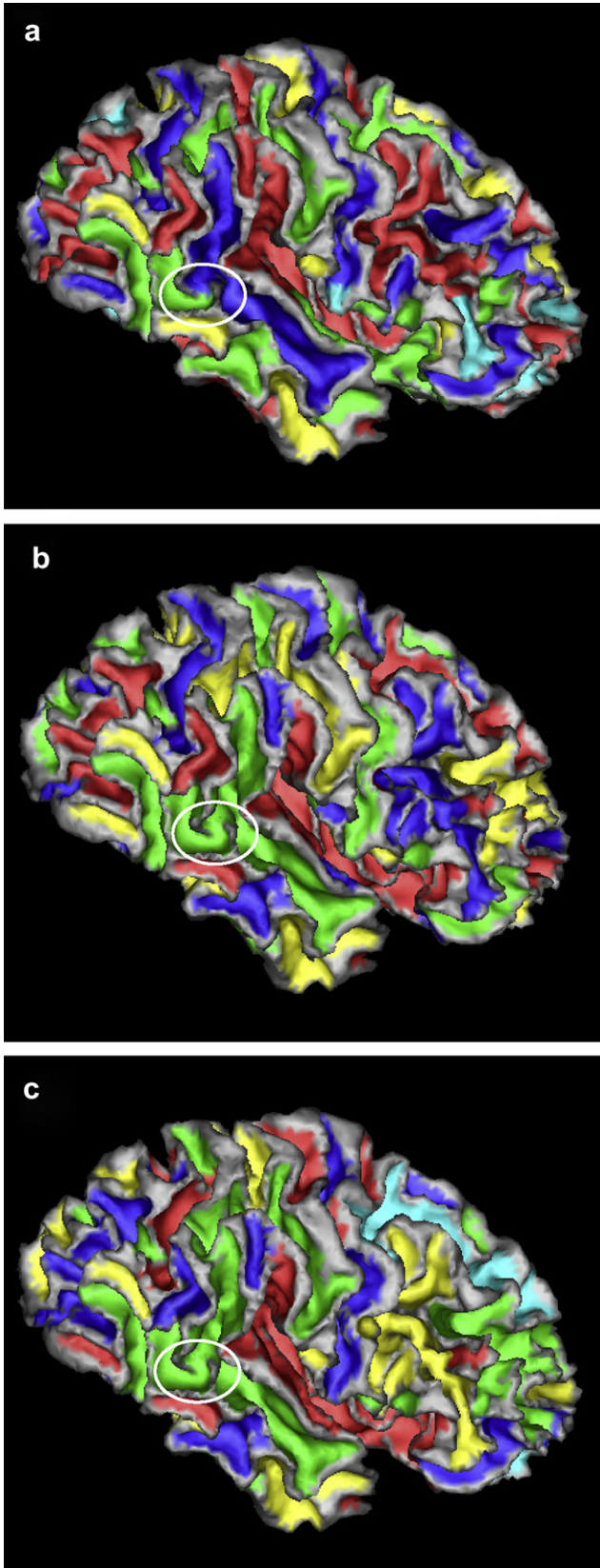
Fig. 5. Effects of the metric selection in the region growing process: (a) geodesic depth; (b) mean curvature; and (c) sulcal class probability. The superior temporal sulcus is connected to other sulci if mean curvature or sulcal probability are used as region growing metrics (refer to the region in white circles).

Our next experiment studied the influence of parameter settings on the final segmentation results. Parameters $\sigma_h^{(0)}$, $\sigma_d^{(0)}$ affect the initial class probabilities (Eqs. (7) and (8)). With constant $T_w = 2.5$ mm, we varied $\sigma_h^{(0)}$ from 0.15 to 0.25 in steps of 0.05; $\sigma_d^{(0)}$ varied from 1.5 to 3.0 in steps of 0.5. The similarity index SI (Dice, 1945) was computed for the segmentation of each sulcus and each pair of the parameter combinations: $\text{SI} = 2n_c/(n_i + n_j)$, where n_i, n_j correspond to the number of vertices of segments

Table 1
Similarity indices in 20 cases for the central (CS), post-central (PCS) and superior temporal sulcus (STS)

	CS	STS	PCS
Avg	0.9260	0.9304	0.9183
Std dev	0.0625	0.0851	0.1006

Table 2
Segmentation results in 20 cases for the central (CS), post-central (PCS) and superior temporal sulcus (STS)

# of anatomical segments	CS (%)		PCS (%)		STS (%)	
	CSR	OSR	CSR	OSR	CSR	OSR
1	80	20	15	15	25	30
2			45	5	30	
3			20		15	

Correct segmentation rate (CSR) and over-segmentation rate (OSR): refer to the text.
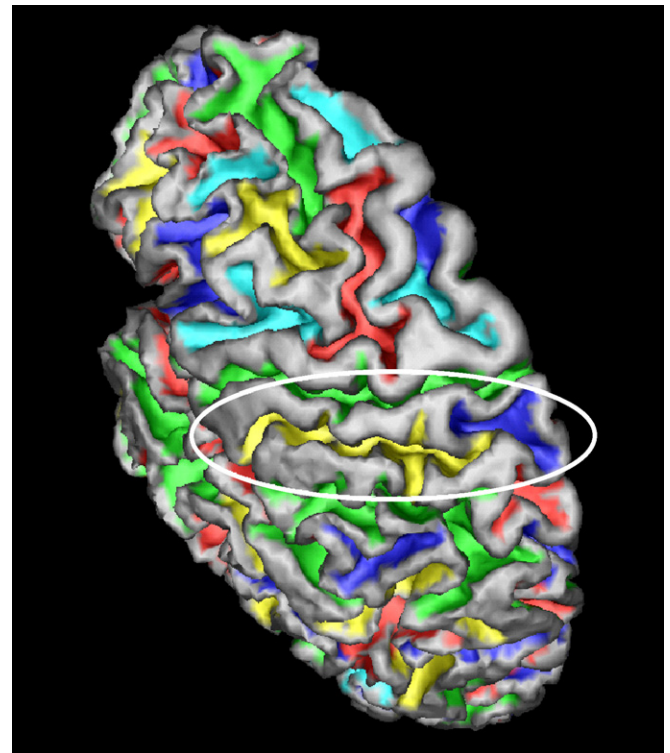

Fig. 6. Sulci segmentation result of a subject. The yellow and blue segments in the white ellipse are the catchment basins making up of the post-central sulcus.

S_i, S_j and n_c is the number of vertices common to S_i and S_j. Higher values SI indicate a greater overlap, or a higher consistency between two segmentation results. The similarity index is not only sensitive to the size of the segmented objects but also to their location. Results listed in Table 1 demonstrate that our method is not affected by the initial choice of $\sigma_h^{(0)}, \sigma_d^{(0)}$.

The watershed threshold T_w has a direct influence on the final segment count: larger values of T_w yield a smaller segment count. We changed T_w from 1 to 20 mm with constant $\sigma_h^{(0)} = 0.2$ and $\sigma_d^{(0)} = 2$. For $T_w > 6$ mm, a serious under-segmentation occurred, which we try to avoid. We prefer a slight over-segmentation, because merging segments is much easier than splitting when matching segments with anatomical labels. Therefore, we empirically selected $T_w = 2.5$ mm for all subsequent experiments.

Next, we wanted to estimate the amount of over-segmentation w.r.t. our final parameter settings in our example group. While the CS is generally anatomically continuous, PCS and STS are often interrupted, i.e., consist of several anatomical segments. We refer to the correct

segmentation rate (CSR) as the proportion of cases where the number of anatomical segments matched the segment count of our algorithm. Likewise, the over-segmentation rate (OSR) is defined.

In Table 2, the CSRs of CS, PCS and STS are 80%, 80% and 70%, respectively. In most of the over-segmen-

Fig. 7. Classification into primary (in red) and secondary (in green) sulci. (a) and (b) are from two different views.
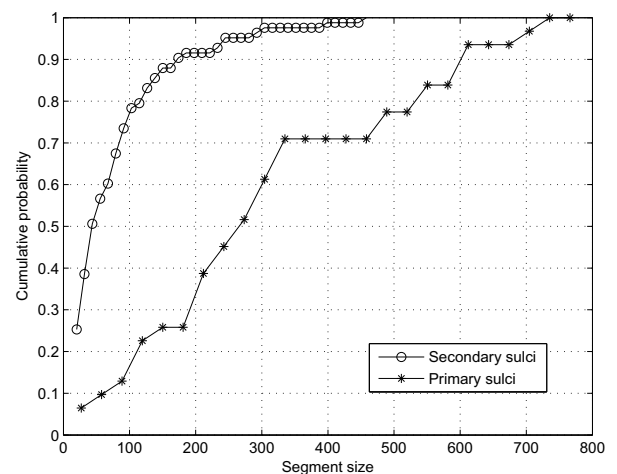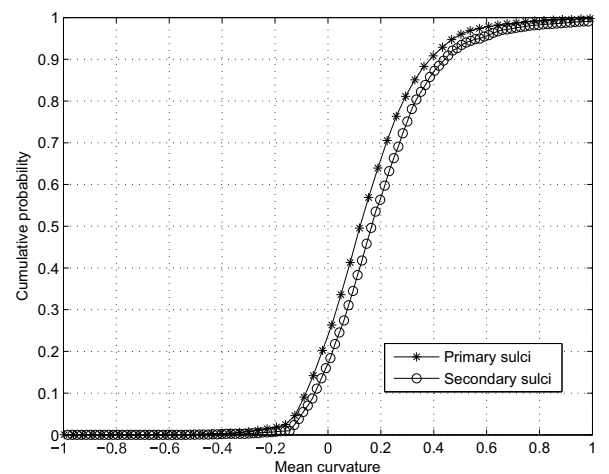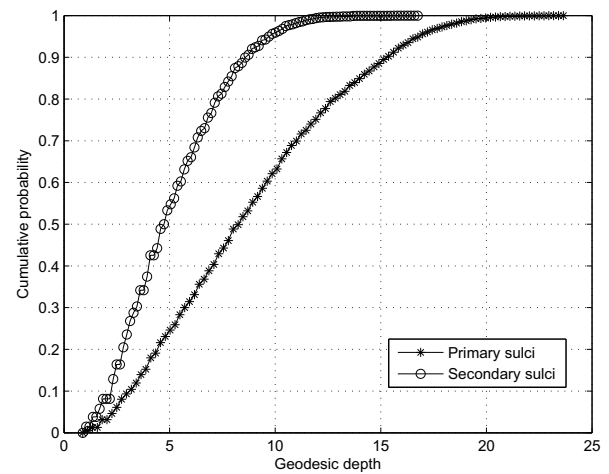

Fig. 8. Cumulative distribution function of geodesic depth (top), mean curvature (middle) and segment size (below) for primary and secondary sulci.
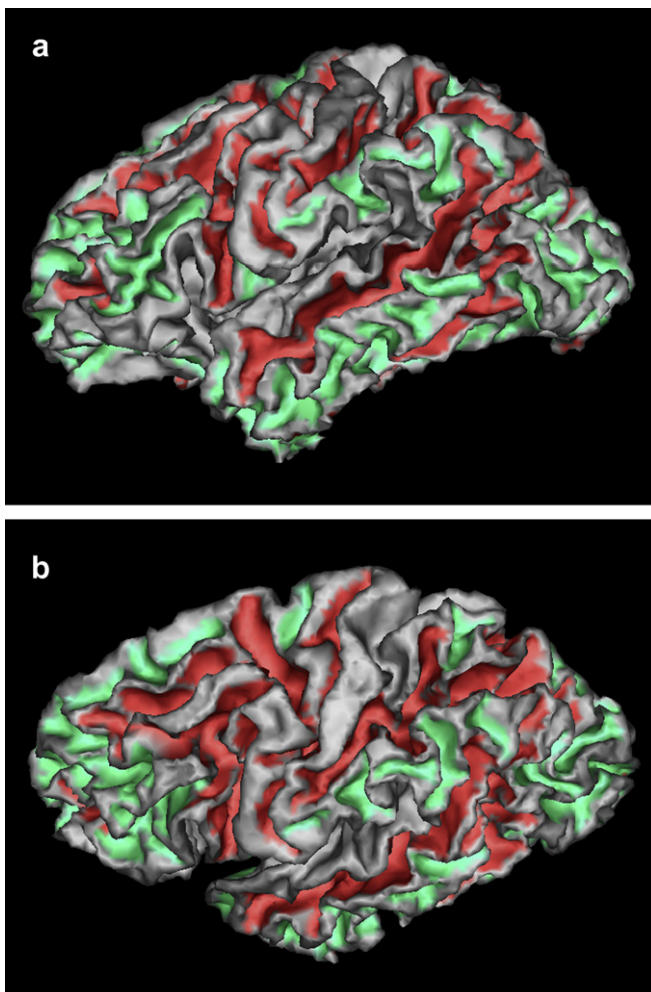
tated cases, small bridging gyri deep in a sulcal fundus led to the formation of separate segments (see Fig. 6). As discussed above, we rather accept a slight over-segmentation.

In our final experiment, we were interested in evaluating differences in geodesic depth and mean curvature for primary and secondary sulci on the lateral surface. Please note all of our other experiments are executed on both lateral and medial surfaces. The reason we exclude the medial surface in this experiment is that some primary sulci on the medial surface (e.g., the cingulate sulcus) are shallower than those on the lateral surface. A k-means classifier based on a histogram of geodesic depth was employed to provide an initial classification of sulci on the lateral aspect (Fig. 7). This initial classification was reviewed by a neuro-anatomist based on the definitions by Ono et al. (1990). From the cumulative probability function in Fig. 8, we find that primary sulci show a greater geodesic depth than secondary sulci – which is very much expected. However, the mean curvature is not apparently different. This is readily understood as a consequence of the fact that the neocortical thickness is rather uniform – and two layers of cortex have to fit into a sulcus, irrespective of its designation as primary or secondary.

To give a visual impression of the segmentation results, we compiled the lateral view of four hemispheres in Fig. 9.

4. Discussion

We proposed a novel, automatic method for segmenting sulci on the cortical surface. The main contributions of our work are (1) using curvature and geodesic depth to segment sulci; (2) deriving a probabilistic theory to combine different information in a Bayesian framework; and (3) comparing the effectiveness of different metrics for the watershed segmentation.

Our work relates to that of Rettmann et al. (2002), who use a deformable surface to distinguish sulci and gyri. Their weights for the internal and external forces w_1, w_2 and distance threshold δ affect the definition of the sulcal area. Larger internal forces w_1 make the deformable surface rigid and will detect a larger area as sulcus. Larger values of δ greatly reduce the detected sulcal area. All these parameters have to be selected empirically.

Here, we start from the first-order approximation that sulci are concave and gyri are convex and use sign of the mean curvature to initialize a classification of vertices. Then, we combine mean curvature and geodesic depth
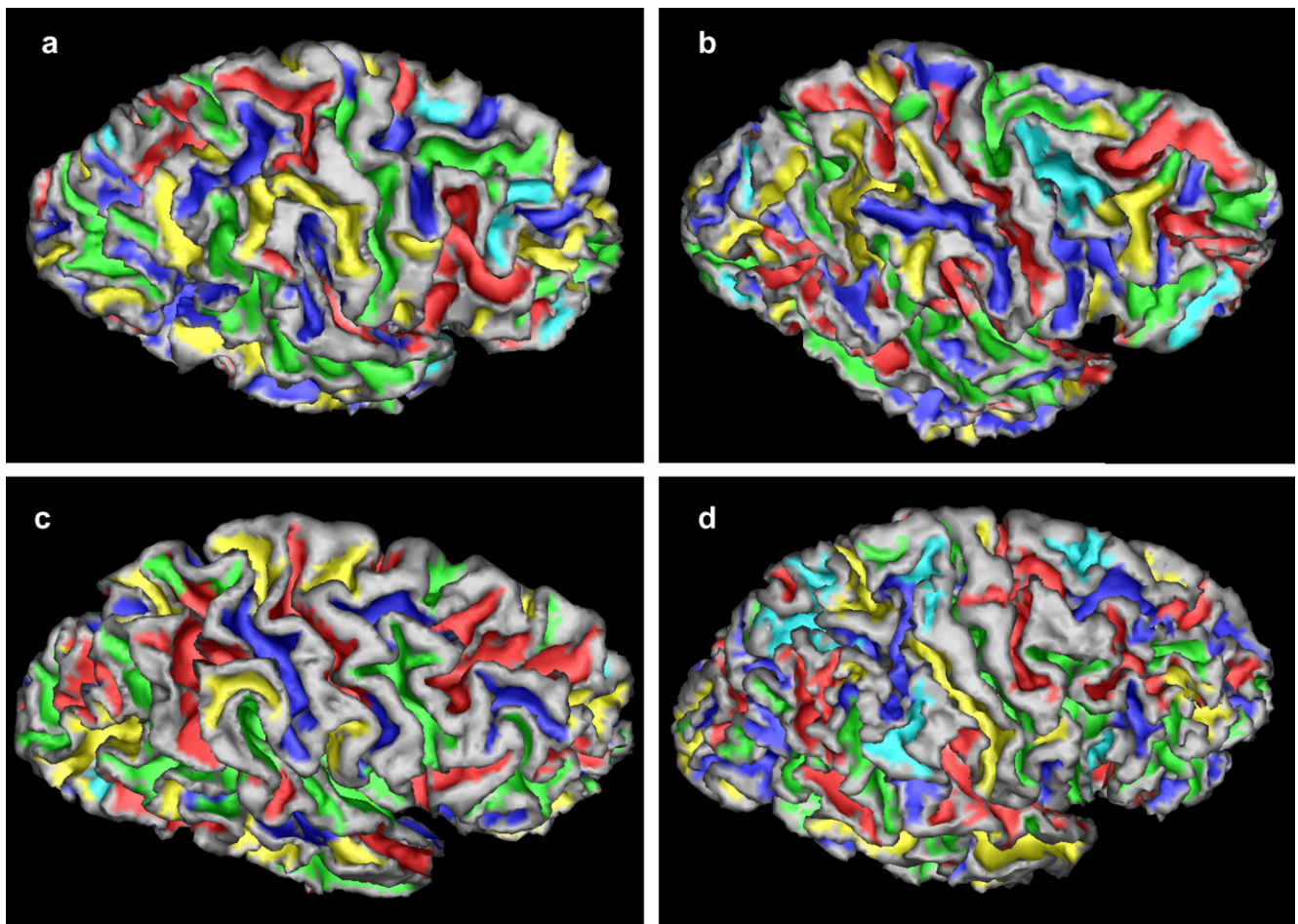

Fig. 9. Segmentation results on the lateral convexity in four subjects.

measures to refine the classification. These parameters are more easily understood in terms of neuroanatomical features, and *ex post* justified from studying their distribution (see Fig. 8).

Cachia et al. (2003) used mean curvature in scale space to detect sulcal roots that appear on the fetal cortex. Using curvature and geodesic depth increases the robustness against structural noise and allows using a simpler segmentation scheme.

Experimental results demonstrate that our method performs well on the lateral surface. We adjusted our segmentation parameters to rather accept a slight over-segmentation rate (about 25%). In a subsequent labeling step, it is easier to merge segments into meaningful anatomical objects than to decide about segment splitting. In a few cases, the segment corresponding to the insula is connected with non-sulcal surface areas on the base of the brain. Here, it is easy to split the segments at the entrance of the sylvian fissure.

We compared properties of primary and secondary sulci. It is readily understood that primary sulci are deeper and larger than secondary ones. However, it is not that apparent both types have a similar mean curvature, thus, the bending radius of the primary and secondary sulci is similar. A simple but likely explanation of this finding is given by the following fact: two layers of neocortex of similar thickness must fit in the fold for both types of sulci, thus, imposing an upper bound for the mean curvature.

Image acquisition parameters, different surface generation methods, and the presence of pathological features (e.g., in neuro-degenerative diseases) affect our preprocessing steps that produce the cortical surface. As long as the cortical surface can be successfully generated, our sulci segmentation framework can be applied to extract the sulcal segments.

The complexity and variability of the human brains poses a great challenge to combine anatomical and functional information from a group of human brains into a brain atlas. One method to address this difficulty is spatial normalization, that is, image-based brain volume warping (Friston et al., 1995; Shen and Davatzikos, 2002). However, current spatial normalization methods are unable to match cortical structures exactly between subjects.

An alternative is to perform matching at a higher (e.g., segment) level. Our aim is to develop an automatic segmentation, matching and interpretation system for the neocortical surface. This tool for the neuroscientist will improve the understanding of the structural organization of the human brain and allow morphometric analysis of brains affected by disease processes. Such a system is comprised of two steps: surface segmentation and matching/labeling of segments to an anatomical model. Here, we focus on sulcal segmentation. The next steps is to find segment correspondences between different subjects by using shape, orientation and neighborhood information.

References

Aarts, E., Korst, J., 1989. Simulated Annealing and Boltzmann Machine. Wiley, New York.

Behnke, K.J., Rettmann, M.E., Pham, D.L., Shen, D., Resnick, S.M., Davatzikos, C., Prince, J., 2003. Automatic classification of sulcal regions of the human brain cortex using pattern recognition. In: Proceedings of SPIE, vol. 5032, pp. 1499–1510.

Borgefors, G., 1984. Distance transforms in arbitrary dimensions. Computer Vision, Graphics, and Image Processing 27, 321–345.

Cachia, A., Mangin, J.-F., Rivière, D., Kherif, F., Boddaert, N., Andrade, A., Papadopoulos-Orfanos, D., Poline, J.-B., Bloch, I., Zilbovicius, M., Sonigo, P., Brunelle, F., Régis, J., 2003. A primal sketch of the cortex mean curvature: a morphogenesis based approach to study the variability of the folding patterns. IEEE Transactions on Medical Imaging 22, 754–765.

Cignoni, P., Ganovelli, F., Montani, C., Scopigno, R., 2000. Reconstruction of topologically correct and adaptive trilinear isosurfaces. Computers and Graphics 24, 399–418.

Desikan, R.S., Ségonne, F., Fischl, B., Quinn, B.T., Dickerson, B.C., Blacker, D., Buckner, R.L., Dale, A.M., Maguire, R.P., Hyman, B.T., Albert, M.S., Killiany, R.J., 2006. An automated labeling system for subdividing the human cerebral cortex on MRI scans into gyral based regions of interest. NeuroImage 31, 968–980.

Dice, L.R., 1945. Measure of the amount of ecologic association between species. Ecology 26, 1037–1044.

Duda, R.O., Hart, P.E., Stork, D.G., 2000. Pattern Classification, second ed. Wiley.

Friston, K., Ashburner, J., Frith, C.D., Poline, J.-B., Heather, J.D., Frackowiak, R.S.J., 1995. Spatial registration and normalisation of images. Human Brain Mapping 2, 165–189.

Goualher, G.L., Barillot, C., Bizais, Y., 1997. Three-dimensional segmentation and representation of cortical sulci using active ribbons. International Journal of Pattern Recognition and Artificial Intelligence 11, 1295–1315.

Goualher, G.L., Procyk, E., Collins, D.L., Venugopal, R., Barillot, C., Evans, A.C., 1999. Automated extraction and variability analysis of sulcal neuroanatomy. IEEE Transactions on Medical Imaging 18, 206–217.

Gumhold, S., Borodin, P., Klein, R., 2004. Intersection free simplification. International Journal of Shape Modeling 9, 155–176.

Han, X., Pham, D.L., Tosun, D., Rettmann, M.E., Xu, C., Prince, J.L., 2004. CRUISE: cortical reconstruction using implicit surface evolution. NeuroImage 23, 997–1012.

Heckbert, P.S., Garland, M., 1999. Optimal triangulation and quadric-based surface simplification. Computational Geometry 14, 49–65.

Kao, C.Y., Hofer, M., Sapiro, G., Stern, J., Rehm, K., Rottenberg, D.A., 2007. A geometric method for automatic extraction of sulcal fundi. IEEE Transactions on Medical Imaging 26, 530–540.

Khaneja, N., Miller, M.I., Grenander, U., 1998. Dynamic programming generation of curves on brain surfaces. IEEE Transactions on Pattern Analysis and Machine Intelligence 20, 1260–1265.

Kirkpatrick, S., Gelatt, C.D., Vecchi, M.P., 1983. Optimization by simulated annealing. Science 220, 671–680.

Kruggel, F., 2005. Techniques in analyzing the neocortial fine-structure. In: Leondes, C.T. (Ed.), Medical Imaging Systems, vol. 5. World Scientific Press, Singapore, pp. 255–279.

Kruggel, F., von Cramon, D.Y., 1999. Alignment of magnetic-resonance brain datasets with the stereotactical coordinate system. Medical Image Analysis 3, 175–185.

Kruggel, F., 2007. MRI-based volumetry of head compartments: normative values of healthy adults. NeuroImage 30, 1–11.

Lohmann, G., 1998. Extracting line representations of sulcal and gyral patterns in MR images of the human brain. IEEE Transactions on Medical Imaging 17, 1040–1048.

Lohmann, G., von Cramon, D.Y., 2000. Automatic labelling of the human cortical surface using sulcal basins. Medical Image Analysis 4, 179–188.

Mangin, J.-F., Frouin, V., Bloch, I., Régis, J., López-Krahe, J., 1995. From 3D magnetic resonance images to structural representations of the cortex topography using topology preserving deformations. Journal of Mathematical Imaging and Vision 5, 297–318.

Maragos, P., Schafer, R.W., 1990. Morphological systems for multidimensional signal processing. Proceedings of the IEEE 78, 690–710.

Meyer, F., Beucher, S., 1990. Morphological segmentation. Journal of Visual Communication and Image Representation 1, 21–46.

Mortenson, M.E., 1985. Geometric Modeling. Wiley, New York.

Ono, M., Kubik, S., Abernathey, C.D., 1990. Atlas of the cerebral sulci. Georg Thieme Verlag, Stuttgart, New York.

Pham, D.L., Prince, J.L., 1999. Adaptive fuzzy segmentation of magnetic resonance images. IEEE Transactions on Medical Imaging 18, 737–752.

Rettmann, M.E., Han, X., Xu, C., Prince, J.L., 2002. Automated sulcal segmentation using watersheds on the cortical surface. NeuroImage 15, 329–344.

Riviére, D., Mangin, J.-F., Papadopoulos-Orfanos, D., Martinez, J.-M., Frouin, V., Régis, J., 2002. Automatic recognition of cortical sulci of the human brain using a congregation of neural networks. Medical Image Analysis 6, 77–92.

Sander, P.T., Zucker, S.W., 1987. Tracing surfaces for surfacing traces. In: Proceedings of the 1st International Conference on Computer Vision, pp. 231–241.

Shattuck, D.W., Leahy, R.M., 2001. Automated graph based analysis and correction of cortical volume topology. IEEE Transactions on Medical Imaging 20, 1167–1177.

Shen, D.G., Davatzikos, C., 2002. HAMMER: hierarchical attribute matching mechanism for elastic registration. IEEE Transactions on Medical Imaging 21, 1421–1439.

Shi, Y., Tu, Z., Reiss A., Dutton R., Lee A.D., Galaburda A., Dinov I., Thompson P.M., Toga A.W., 2007. Joint sulci detection using graphical models and boosted priors. In: Proceedings of the IPMI, pp. 98–109.

Stokely, E.M., Wu, S.Y., 1992. Surface parameterization and curvature measurement of arbitrary 3-D objects: five practical methods. IEEE Transactions on Pattern Analysis and Machine Intelligence 14, 833–840.

Toriwaki, J., Yonekura, T., 2002. Euler number and connectivity indexes of a three dimensional digital picture. Forma 17, 183–209.

Vaillant, M., Davatzikos, C., 1997. Finding parametric representations of the cortical sulci using an active contour model. Medical Image Analysis 1, 295–315.

Vivodtzev, F., Linsen, L., Bonneau, G.-P., Hamann, B., Joy, K.I., Olshausen, B.A., 2003. Hierarchical isosurface segmentation based on discrete curvature. Joint Eurographics – IEEE Symposium on Visualization, 249–258.

Xu, C., Prince, J.L., 1998. Snakes, shapes, and gradient vector flow. IEEE Transactions on Image Processing 7, 359–369.

Zhou, Y., Thompson, P.M., Toga, A.W., 1999. Extracting and Representing the cortical sulci. IEEE Computer Graphics and Applications 19, 49–55.